Submitted to the Astrophysical Journal
Preprint typeset using LaTeX style emulateapj v. 11/26/04

FIVE-YEAR WILKINSON MICROWAVE ANISOTROPY PROBE (WMAP[1]) OBSERVATIONS: BAYESIAN ESTIMATION OF CMB POLARIZATION MAPS

J. Dunkley [2,3,4], D. N. Spergel [3,5], E. Komatsu [6], G. Hinshaw [9], D. Larson [8], M. R. Nolta [7], N. Odegard [10], L. Page [2], C. L. Bennett [8], B. Gold [8], R. S. Hill [10], N. Jarosik [2], J. L. Weiland [10], M. Halpern [11], A. Kogut [9], M. Limon [12], S. S. Meyer [13], G. S. Tucker [14], E. Wollack [9], E. L. Wright [15]

Submitted to the Astrophysical Journal

ABSTRACT

We describe a sampling method to estimate the polarized CMB signal from observed maps of the sky. We use a Metropolis-within-Gibbs algorithm to estimate the polarized CMB map, containing Q and U Stokes parameters at each pixel, and a marginalized covariance matrix. These can be used as inputs for cosmological analyses. The polarized sky signal is parameterized as the sum of three components: CMB, synchrotron emission, and thermal dust emission. The polarized Galactic components are modeled with spatially varying power law spectral indices for the synchrotron, and a fixed power law for the dust, and their component maps are estimated as by-products. We apply the method to simulated low resolution maps with pixels of side 7.2 degrees, using diagonal and full noise realizations drawn from the *WMAP* inverse noise matrices. The CMB maps are recovered with goodness of fit consistent with errors. Computing the likelihood of the E-mode power in the maps as a function of optical depth to reionization, τ, for fixed temperature anisotropy power, we recover $\tau = 0.091 \pm 0.019$ for a simulation with input $\tau = 0.1$, and mean $\tau = 0.098$ averaged over 10 simulations. A 'null' simulation with no polarized CMB signal has maximum likelihood consistent with $\tau = 0$. The method is applied to the five-year *WMAP* data, using the K, Ka, Q and V channels. We find $\tau = 0.090 \pm 0.019$, compared to $\tau = 0.086 \pm 0.016$ from the template-cleaned maps used in the primary *WMAP* analysis. The synchrotron spectral index, β, averaged over high signal-to-noise pixels with standard deviation $\sigma(\beta) < 0.25$, but excluding $\sim 6\%$ of the sky masked in the Galactic plane, is -3.02 ± 0.04. This estimate does not vary significantly with Galactic latitude and depends only weakly on the choice of spectral index prior.

Subject headings: cosmic microwave background, cosmology: observations, methods: statistical, polarization, radio continuum: ISM

1. INTRODUCTION

The *Wilkinson Microwave Anisotropy Probe* (*WMAP*) has mapped the sky in five frequency bands between 23 and 94 GHz. Measurements of the temperature anisotropy in the CMB have led to the establishment of the ΛCDM cosmological model. Anisotropies in the CMB polarization at large scales inform us about the ionization history of the universe, allow us to probe a possible signal from gravitational waves seeded early in the universe, and lead to improved constraints on cosmological parameters when combined with temperature measurements. The three-year *WMAP* observations (Page et al. 2007) showed that polarized diffuse emission from our Galaxy dominates the primordial signal over much of the sky, making accurate estimation of the CMB signal at large angular scales challenging.

In this paper we describe a Bayesian framework for estimating the low resolution polarized CMB maps, and errors marginalized over possible Galactic emission. The goal of this approach is to determine not only the 'best' estimate of the microwave background polarization fluctuations but to determine the uncertainties associated with foreground removal. A similar technique has also been developed by Eriksen et al. (2006, 2007) for estimating intensity maps, and has been applied to the three-year *WMAP* temperature maps. This is one of a set of related papers on the five-year *WMAP* analysis. Hinshaw et al. (2008) report on data processing and basic results, Hill et al. (2008) on beam models and window functions, Gold et al. (2008) on unpolarized and

[1] *WMAP* is the result of a partnership between Princeton University and NASA's Goddard Space Flight Center. Scientific guidance is provided by the *WMAP* Science Team.

[2] Dept. of Physics, Jadwin Hall, Princeton University, Princeton, NJ 08544-0708
[3] Dept. of Astrophysical Sciences, Peyton Hall, Princeton University, Princeton, NJ 08544-1001
[4] Astrophysics, University of Oxford, Keble Road, Oxford, OX1 3RH, UK
[5] Princeton Center for Theoretical Physics, Princeton University, Princeton, NJ 08544
[6] Univ. of Texas, Austin, Dept. of Astronomy, 2511 Speedway, RLM 15.306, Austin, TX 78712
[7] Canadian Institute for Theoretical Astrophysics, 60 St. George St, University of Toronto, Toronto, ON Canada M5S 3H8
[8] Dept. of Physics & Astronomy, The Johns Hopkins University, 3400 N. Charles St., Baltimore, MD 21218-2686
[9] Code 665, NASA/Goddard Space Flight Center, Greenbelt, MD 20771
[10] Adnet Systems, Inc., 7515 Mission Dr., Suite A1C1 Lanham, Maryland 20706
[11] Dept. of Physics and Astronomy, University of British Columbia, Vancouver, BC Canada V6T 1Z1
[12] Columbia Astrophysics Laboratory, 550 W. 120th St., Mail Code 5247, New York, NY 10027-6902
[13] Depts. of Astrophysics and Physics, KICP and EFI, University of Chicago, Chicago, IL 60637
[14] Dept. of Physics, Brown University, 182 Hope St., Providence, RI 02912-1843
[15] PAB 3-909, UCLA Physics & Astronomy, PO Box 951547, Los Angeles, CA 90095–1547
Electronic address: j.dunkley@physics.ox.ac.uk

polarized Galactic emission, and Wright et al. (2008) on emission from extra-Galactic point sources. The angular power spectra are described in Nolta et al. (2008), cosmological parameter constraints from *WMAP* data in Dunkley et al. (2008), and interpretation of cosmological constraints in Komatsu et al. (2008). This work complements the primary analysis of the *WMAP* polarization maps described in Gold et al. (2008), which uses template cleaning to estimate the CMB polarization maps.

This paper is structured as follows. In §2 we describe the sampling method used to estimate polarized maps. In §3 we apply it to simulated maps, and in §4 to the *WMAP* data. We conclude in §5.

2. ESTIMATION OF POLARIZATION MAPS

The large-scale polarized radiation observed by *WMAP* is the sum of at least three components: the primordial CMB, synchrotron emission, and thermal dust emission. Here we briefly review the Galactic emission mechanisms, for more details see e.g., Page et al. (2007). Both synchrotron and thermal dust emission are polarized due to the Galactic magnetic field, measured to have a coherent spiral structure parallel to the Galactic plane, as well as a significant turbulent component (Spitzer 1998; Beck 2001; Vallée 2005; Han 2006). The effective strength of the field is of order $\sim 10\ \mu$G, thought to be split roughly equally between the coherent and turbulent components (Crutcher et al. 2003). Synchrotron emission is produced by relativistic cosmic-ray electrons accelerated in this magnetic field (see Strong et al. (2007) for a review of cosmic ray propagation). For electrons with a power law distribution of energies

$$N(E) \propto E^{-p}, \tag{1}$$

the frequency dependence of the emission is characterized by antenna temperature $T(\nu) \propto \nu^{\beta}$ with spectral index $\beta = -(p+3)/2$, with typically $\beta \sim -3$ (Rybicki & Lightman 1979). However, since synchrotron loss is proportional to E^2, older sources of electrons should have a lower energy distribution and a steeper spectral index of synchrotron emission, compared to regions of recently injected electrons. This leads to a synchrotron index that varies over the sky (Lawson et al. 1987; Reich & Reich 1988) and is expected to steepen away from the Galactic plane (Strong et al. 2007), with evidence of this behavior seen in the *WMAP* data (Bennett et al. 2003). Since the cosmic-ray electrons emit radiation almost perpendicular to the Galactic magnetic field in which they orbit, they can produce polarization fractions as high as $\sim 75\%$ (Rybicki & Lightman 1979), although integration of multiple field directions along a line of sight reduces this level. The fractional polarization observed at radio frequencies in the range 408 MHz - 2.4 GHz is further lowered due to Faraday rotation (Duncan et al. 1995; Uyaniker et al. 1999; Wolleben et al. 2006). In the WMAP 23 GHz data, the polarization fraction is as high as 50% on significant portions of the sky (Kogut et al. 2007).

Thermal dust intensity has been well measured by the *IRAS* and *COBE* missions and extrapolated to microwave frequencies by Finkbeiner et al. (1999). Polarization arises since grains tend to align their long axes perpendicular to the Galactic magnetic field via, for example, the Davis-Greenstein mechanism (Davis & Greenstein 1951), and depending on their composition can be polarized up to a modeled maximum of $\sim 20\%$ parallel to the long axes (e.g., Hildebrand & Dragovan (1995); Draine & Fraisse (2008)). Observations of starlight, polarized perpendicular to the dust grains, are consistent with this picture (Heiles 2000; Berdyugin et al. 2001), as are the three-year *WMAP* observations (Page et al. 2007; Kogut et al. 2007). A population of smaller spinning dust grains formed of polycyclic aromatic hydrocarbons may also emit a significant amount of microwave radiation due to electric dipole rotational emission (Draine & Lazarian 1999; Draine & Li 2007). This question is discussed in e.g. Hinshaw et al. (2007); Dobler & Finkbeiner (2007); Gold et al. (2008) with respect to the intensity signal observed by *WMAP*. However, these small spinning dust grains are not expected to be significantly polarized (Draine 2003). Other mechanisms for producing polarized emission, including magnetic dust (Draine & Lazarian 1999), have not been observed to be dominant.

Given these polarized Galactic components, the standard method used to clean the *WMAP* polarization maps involves subtracting synchrotron and dust template maps from the total, leaving a cleaned CMB map at the Ka, Q, and V bands (Page et al. 2007; Gold et al. 2008). The spectral indices of the templates are not allowed to vary spatially, which is a sufficient approximation given the sensitivity of the observations. Errors are propagated by marginalizing the noise matrices over the uncertainties in the fitted coefficients of template maps (Page et al. 2007). In this alternative method we parameterize the emission model, and use a sampling method to estimate the marginalized CMB Q and U maps in low resolution pixels.

2.1. *Bayesian estimation of sky maps*

The data, $\mathbf{d}$, consist of the Q and U polarization maps observed by *WMAP* at N_c frequency channels, and is a vector of length $2N_p \times N_c$. In this analysis we will use HEALPix $N_{\rm side}$=8 with $N_p = 768$ [16]. The joint posterior distribution for a model $\mathbf{m}$ can be written as

$$p(\mathbf{m}|\mathbf{d}) \propto p(\mathbf{d}|\mathbf{m})p(\mathbf{m}), \tag{2}$$

with prior distribution $p(\mathbf{m})$ and Gaussian likelihood

$$-2\ln p(\mathbf{d}|\mathbf{m}) = \chi^2 + c, \tag{3}$$

with

$$\chi^2 = (\mathbf{d}-\mathbf{m})^T\mathbf{N}^{-1}(\mathbf{d}-\mathbf{m}) \tag{4}$$

and a normalization term c. Since the noise $\mathbf{N}$ is uncorrelated between channels, the likelihood can be written as the sum over frequency ν,

$$\chi^2 = \sum_{\nu}[\mathbf{d}_\nu - \mathbf{m}_\nu]^T\mathbf{N}_\nu^{-1}[\mathbf{d}_\nu - \mathbf{m}_\nu], \tag{5}$$

where $\mathbf{N}_\nu$ is the noise covariance at each channel. In this analysis we use *WMAP* low resolution maps with inverse noise matrices that are not defined inside a processing mask covering $\sim 6\%$ of the sky. Instead of omitting these pixels, we set the diagonal elements of N_ν^{-1} in the masked pixels to be small.

[16] The number of pixels is $N_p = 12N_{\rm side}^2$, with $N_{\rm side} = 2^{\rm res}$ where res is the 'resolution' (Gorski et al. 2005).

We parameterize the model in antenna temperature as the sum of three components:

$$\mathbf{m}_\nu = \sum_k \boldsymbol{\alpha}_{k,\nu}\mathbf{A}_k, \tag{6}$$

with CMB (k=1), synchrotron emission (k=2), and thermal dust emission (k=3). In this analysis we will ignore possible polarized contributions from other components including spinning dust, and free-free emission. Free-free emission may become slightly polarized due to Thomson scattering by electrons in HII regions.

The components each have amplitude vectors $\mathbf{A}_k$ of length $2N_p$ and diagonal coefficient matrices $\boldsymbol{\alpha}_{k,\nu}$ of side $2N_p$ at each frequency. The CMB radiation is blackbody, and we further assume that the Galactic components can be described with a spectral index that does not vary with frequency in the *WMAP* range. The coefficients are therefore given by

$$\boldsymbol{\alpha}_{1,\nu} = f(\nu)\mathbf{I}, \tag{7}$$

$$\boldsymbol{\alpha}_{2,\nu} = \mathrm{diag}[(\nu/\nu_K)^{\boldsymbol{\beta}_2}], \tag{8}$$

$$\boldsymbol{\alpha}_{3,\nu} = \mathrm{diag}[(\nu/\nu_W)^{\boldsymbol{\beta}_3}]. \tag{9}$$

Here we have introduced two spectral index vectors $\boldsymbol{\beta}_k$ each of length $2N_p$, pivoted at 23 GHz (ν_K) and 94 GHz (ν_W) respectively. The function $f(\nu)$ converts thermodynamic to antenna temperature. We then make three further simplifying assumptions. First, that the spectral indices in Q and U are the same in a given pixel, which equates to assuming that the polarization angle does not change with frequency. Second, the spectrum of thermal dust is assumed to be fixed over the sky, with fiducial value $\boldsymbol{\beta}_d = 1.7$, motivated by Finkbeiner et al. (1999). Third, we define $N_i < N_p$ pixels within which β_2 takes a common value, rather than allow it to take a unique value at each N_{side}=8 pixel. This is motivated by our understanding of the emission process: even though we expect spatial variation due to the different ages of the electron populations, the electron diffusion rate limits how much the index can vary over a short range (Strong et al. 2000, 2007). In this case we use N_{side}=2 HEALPix pixels ($N_i = 48$).

Our model $\mathbf{m}$ is now described by $6N_p$ amplitude parameters $\mathbf{A} = (\mathbf{A}_1, \mathbf{A}_2, \mathbf{A}_3)^T$ and N_i spectral index parameters $\boldsymbol{\beta}$. Our main objective is to estimate the marginalized distribution for the CMB amplitude vector,

$$p(\mathbf{A}_1|\mathbf{d}) = \int p(\mathbf{A}, \boldsymbol{\beta}|\mathbf{d}) d\mathbf{A}_2 d\mathbf{A}_3 d\boldsymbol{\beta}, \tag{10}$$

from which we can estimate a map and covariance matrix.

2.2. *Sampling the distribution*

We cannot sample the joint distribution $p(\mathbf{A}, \boldsymbol{\beta}|\mathbf{d})$ directly, so we use Markov Chain Monte Carlo methods to draw samples from it. It can be sliced into two conditional distributions $p(\mathbf{A}|\boldsymbol{\beta}, \mathbf{d})$ and $p(\boldsymbol{\beta}|\mathbf{A}, \mathbf{d})$, so we use Gibbs sampling to draw alternately from each conditional distribution, constructing a Markov chain with the desired joint distribution as its stationary distribution.

We briefly review Gibbs sampling for the case of one A parameter and one β parameter: starting from an arbitrary point (A_i, β_i) in the parameter space, we draw

$$(A_{i+1}, \beta_{i+1}), (A_{i+2}, \beta_{i+2})... \tag{11}$$

by first drawing A_{i+1} from $p(A|\beta_i, d)$ and then drawing β_{i+1} from $p(\beta|A_{i+1}, d)$. Then we iterate many times. The result is a Markov chain whose stationary distribution is $p(A, \beta|d)$. A description of Gibbs sampling can be found in Gelfand & Smith (1990), Wandelt et al. (2004), and Eriksen et al. (2007).

For the multivariate case $\mathbf{A}$ and $\boldsymbol{\beta}$ are now vectors, and so each vector is drawn in turn until convergence, producing a chain whose stationary distribution is the joint posterior distribution. Two distinct methods are used to draw the samples from each conditional distribution, depending on whether the amplitude vector $\mathbf{A}$, or the index vector $\boldsymbol{\beta}$, is held fixed.

2.2.1. *Sampling the amplitude vector*

For fixed $\boldsymbol{\beta}$, the conditional distribution $p(\mathbf{A}|\boldsymbol{\beta}, \mathbf{d})$ is a $6N_p$-dimensional Gaussian, so one can draw a sample of all $6N_p$ amplitude parameters simultaneously. The conditional distribution is

$$p(\mathbf{A}|\boldsymbol{\beta}, \mathbf{d}) \propto p(\mathbf{d}|\boldsymbol{\beta}, \mathbf{A})p(\mathbf{A}). \tag{12}$$

For a uniform prior on $\mathbf{A}$, the mean, $\hat{\mathbf{A}}$, is found by minimizing

$$\chi^2 = \sum_\nu [\mathbf{d}_\nu - \sum_k \boldsymbol{\alpha}_{k,\nu}\mathbf{A}_k]^T \mathbf{N}_\nu^{-1} [\mathbf{d}_\nu - \sum_k \boldsymbol{\alpha}_{k,\nu}\mathbf{A}_k] \tag{13}$$

with respect to $\mathbf{A}$. This gives $\hat{\mathbf{A}} = \mathbf{F}^{-1}\mathbf{x}$, which can be written in block-matrix form,

$$\begin{pmatrix} \hat{\mathbf{A}}_1 \\ \hat{\mathbf{A}}_2 \\ \hat{\mathbf{A}}_3 \end{pmatrix} = \begin{pmatrix} \mathbf{F}_{11} & \mathbf{F}_{12} & \mathbf{F}_{13} \\ \mathbf{F}_{21} & \mathbf{F}_{22} & \mathbf{F}_{23} \\ \mathbf{F}_{31} & \mathbf{F}_{32} & \mathbf{F}_{33} \end{pmatrix}^{-1} \begin{pmatrix} \mathbf{x}_1 \\ \mathbf{x}_2 \\ \mathbf{x}_3 \end{pmatrix} \tag{14}$$

with elements

$$\mathbf{F}_{kk'} = \sum_\nu \boldsymbol{\alpha}_{k,\nu}^T \mathbf{N}_\nu^{-1} \boldsymbol{\alpha}_{k',\nu}, \tag{15}$$

$$\mathbf{x}_k = \sum_\nu \boldsymbol{\alpha}_{k,\nu}^T \mathbf{N}_\nu^{-1} \mathbf{d}_\nu. \tag{16}$$

Note that $\mathbf{F}$ is a $2N_p \times 2N_p$ matrix and $\mathbf{x}$ is a vector of length $2N_p$. The covariance of the conditional distribution is given by $\mathbf{F}^{-1}$. In the case of diagonal noise, the mean and variance are estimated pixel by pixel using the same method. Given the mean and Fisher matrix of the conditional distribution, we draw a Gaussian sample using the lower Cholesky decomposition of the Fisher matrix, $\mathbf{F} = \mathbf{L}\mathbf{L}^T$, with sample $\mathbf{A}_{i+1} = \hat{\mathbf{A}} + \mathbf{L}^{-1}\mathbf{G}$. The vector $\mathbf{G}$ contains $2N_p$ zero mean unit variance Gaussian random samples.

For a diagonal Gaussian prior on $A_{x,k}$ of $a_k \pm \sigma_k$, the expressions are modified to

$$\tilde{\mathbf{F}}_{kk'} = \mathbf{F}_{kk'} + \delta_{kk'}\sigma_k^{-2}\mathbf{I}, \tag{17}$$

$$\tilde{\mathbf{x}}_k = \mathbf{x}_k + \sigma_k^{-2}\mathbf{I}\mathbf{a}_k, \tag{18}$$

with posterior mean $\hat{\mathbf{A}} = \tilde{\mathbf{F}}^{-1}\tilde{\mathbf{x}}$ and variance $\tilde{\mathbf{F}}^{-1}$. In this analysis we place uniform priors on the CMB and synchrotron Q and U amplitudes at each pixel, but impose a Gaussian prior on the dust Stokes vector $\mathbf{A}_2 = (\mathbf{Q}_2, \mathbf{U}_2)^T$ of $[\mathbf{Q}_2, \mathbf{U}_2] = 0 \pm 0.2\ \mathbf{I}_d$, using the dust map $\mathbf{I}_d$ at 94 GHz from model 8 of Finkbeiner et al. (1999), hereafter FDS, as a tracer of the intensity. The width of the prior, corresponding to a polarization fraction 20%, is motivated by Draine & Fraisse (2008), who predict the maximum polarization of dust grains to be about 15%.

Drawing this new amplitude vector is computationally demanding, and drives us to work with low resolution maps. Our goal is to determine the polarized CMB signal at large angular scale, so this does not limit the analysis.

2.2.2. *Sampling the index vector*

For fixed A, we sample from the conditional distribution

$$p(\boldsymbol{\beta}|\mathbf{A},\mathbf{d}) \propto p(\mathbf{d}|\boldsymbol{\beta},\mathbf{A})p(\boldsymbol{\beta}), \tag{19}$$

with prior probability $p(\boldsymbol{\beta})$. An analytic sample cannot be drawn from this distribution because the spectral indices are non-linear parameters. However, for a small number of parameters it is feasible to draw samples using the Metropolis-Hastings algorithm. This algorithm has been described extensively in the cosmological parameter estimation literature (e.g., Knox et al. (2001); Lewis & Bridle (2002); Dunkley et al. (2005)). The sampling goes as follows. For each index parameter in turn, a trial step β_T is drawn using a Gaussian proposal distribution of width σ_T centered on the current $\boldsymbol{\beta}$ vector. Next, the current and trial $\boldsymbol{\beta}$ vectors are used to construct model vectors at each frequency, $\mathbf{m}_\nu = \sum_k \boldsymbol{\alpha}_{k,\nu}\mathbf{A}_k$. The current and trial posterior are then computed using

$$-2\ln p(\boldsymbol{\beta}|\mathbf{A},\mathbf{d}) = \chi^2 - 2\ln p(\boldsymbol{\beta}), \tag{20}$$

with χ^2 given in Eqn 5. The ratio of the trial to current posterior, r, is used to determine whether to move to the trial position (with probability r), or to stay at the original position (with probability $1-r$). This use of the Metropolis algorithm to draw a subset of parameters is commonly known as Metropolis-within-Gibbs (e.g. Geweke & Tanizaki (2001)), and has been used in astronomy to estimate Cepheid distances (Barnes et al. 2003). Other approaches to sampling spectral index parameters have been considered in e.g., Eriksen et al. (2007).

In regions of low signal-to-noise, it is necessary to impose a prior on the synchrotron spectral index, otherwise it is unconstrained and could take the 'flat' index of the CMB component, opening up large degeneracies. We choose a Gaussian prior of -3.0 ± 0.3, motivated by understanding of the synchrotron emission (Rybicki & Lightman 1979) and allowing for variations of the size observed in the synchrotron intensity (e.g., Bennett et al. (2003)). This is combined with a uniform prior on the CMB and synchrotron amplitudes, and a Gaussian prior $0 \pm 0.2 I_d$ on the dust Q and U amplitudes. This parameterization and choice of prior does not guarantee that the marginalized means for the A and β parameters will be unbiased estimators. In the limit of low signal-to-noise, there is a larger volume of models with a flatter (i.e. β tending to 0) synchrotron spectrum, allowing large CMB and synchrotron amplitudes of opposite sign. A solution is to impose an additional 'phase-space' prior on the spectral indices, so that the marginalized means are unbiased. We discuss this further in §3, using simulations to test the parameter bias.

2.3. *Processing the sampled distribution*

We form maps of each component from the mean of the marginalized distribution,

$$\langle \mathbf{A}_k \rangle = \int p(\mathbf{A}_k|\mathbf{d})\mathbf{A}_k d\mathbf{A}_k = \frac{1}{n_\mathrm{G}} \sum_{i=1}^{n_\mathrm{G}} \mathbf{A}_k^i, \tag{21}$$

where the sum is over all n_G elements in the chain, and $\mathbf{A}_k^i$ is the ith chain element of the kth component map. The covariance matrices for $\mathbf{A}_k$, including off-diagonal terms, are estimated using the same method, summing over the chain components. As an example, the covariance $C_{xy,k}$ between pixels x and y for component k is computed using

$$C_{xy,k} = \langle A_{x,k}A_{y,k}\rangle - \langle A_{x,k}\rangle\langle A_{y,k}\rangle \tag{22}$$

$$= \frac{1}{n_\mathrm{G}} \sum_{i=1}^{n_\mathrm{G}} (A_{x,k}^i - \langle A_{x,k}\rangle)(A_{y,k}^j - \langle A_{y,k}\rangle). \tag{23}$$

For the synchrotron and dust components, we compute only the diagonal elements of the covariance matrices.

2.3.1. *Power in the E-mode*

To quantify the polarization anisotropy present in the Q and U maps, we use the coordinate-independent scalar and pseudo-scalar E and B modes commonly used in cosmological analysis (Seljak 1997; Kamionkowski et al. 1997). Both polarization modes probe the evolution of the decoupling and reionization epochs and are generated by Thomson scattering of a quadrupolar radiation pattern by free electrons. The anisotropy is quantified using the C_ℓ^{TE}, C_ℓ^{EE}, C_ℓ^{BB} power spectra, where

$$C_\ell^{XY} = \langle a_{lm}^X a_{lm}^{Y*}\rangle. \tag{24}$$

The spin-2 decomposition of the polarization maps, $a_{lm}^{E,B}$, is related to the Q and U maps by

$$[Q \pm iU](\hat{x}) = \sum_{\ell>1} \sum_{m=-\ell}^{\ell} {}_{\mp2}a_{\ell m}\, {}_{\mp2}Y_{\ell m}(\hat{x}) \tag{25}$$

where ${}_{\pm2}a_{lm} = a_{lm}^E \pm i a_{lm}^B$ (Zaldarriaga & Seljak 1997).

The first stars reionize the universe at redshift z_r, producing a signal in the E-mode power spectrum proportional to τ^2, where τ is the optical depth to reionization. In this analysis we use the approximation to the optical depth used in Page et al. (2007), estimated by varying only τ and the power spectrum amplitude, such that the temperature anisotropy power at $\ell = 220$ is held constant. Other cosmological parameters are fixed to fiducial values and the exact likelihood is computed as a function of τ. The likelihood, $p(C_\ell|\mathbf{d})$, given in Appendix D of Page et al. (2007), is evaluated using the marginalized Q/U map and covariance matrix, which are processed as described in Page et al. (2007) to account for the P06 Galactic mask.

2.4. *Testing convergence*

The convergence of the chain is determined by applying the spectral convergence test described in Dunkley et al. (2005) to the spectral index parameters and a random subset of the amplitude parameters. This tests for convergence of the mean, but convergence of the covariance matrix is also required for estimating the power in the mapx at large scales. We check this by applying a jackknife test to the derived optical depth parameter τ. For a chain that samples only the amplitude vectors, and has diagonal noise, 1000 iterations are typically sufficient. With the Metropolis sampling step included, about 10,000 iterations are required, and when off-diagonal noise is included, typically 50,000 iterations are necessary.

3. SIMULATED POLARIZATION MAPS

We simulate all-sky signal and noise maps at HEALPix $N_{\rm side}$=16, with $N_p = 3072$ pixels, for the Stokes Q and U parameters, at the five *WMAP* frequencies (22.8, 33, 40.7, 60.8, and 93.5 GHz). In the notation of §2, the data are modeled as

$$\mathbf{s}_\nu = f(\nu)\mathbf{A}_1 + (\nu/\nu_K)^{\beta_s}\mathbf{A}_2 + (\nu/\nu_W)^{\beta_d}\mathbf{A}_3, \qquad (26)$$

where $\mathbf{s}_\nu$ is a vector of length $2N_p$ containing the total Q and U signal in antenna temperature at frequency ν. The CMB signal map, $\mathbf{A}_1$, is generated for a fiducial cosmological model by drawing multipoles a_{lm} from the theoretical power spectrum C_ℓ, and transforming to map space, using the 'synfast' routine in HEALPix. We choose a model with $\tau = 0.1$, with other cosmological parameters given by the best-fit three-year *WMAP* ΛCDM model (Spergel et al. 2007). For the synchrotron emission, with amplitude map $\mathbf{A}_2$ defined at 23 GHz, we use the three-year *WMAP* Q and U low-resolution K-band maps (Page et al. 2007). The frequency dependence is assumed to be a power law with $\beta = -3.0$ over the full sky. For the thermal dust map, $\mathbf{A}_3$, defined at W band (94 GHz), we construct maps that are 5% polarized, using the dust intensity template $\mathbf{I}_d$ from IRAS, extrapolated to 94 GHz using Model 8 of Finkbeiner et al. (1999) and degraded to $N_{\rm side}$=16. We form

$$\mathbf{Q}_3 = 0.05\mathbf{I}_d \cos(2\gamma) \qquad (27)$$

$$\mathbf{U}_3 = 0.05\mathbf{I}_d \sin(2\gamma), \qquad (28)$$

where the polarization angles γ are computed from the starlight polarization template described in Page et al. (2007), using observations from Heiles (2000); Berdyugin et al. (2001, 2004). We assume a power law index with $\beta_d = 1.7$ over the whole sky. This is a simplified model of the true sky, as we would expect the emission processes to result in some spatial and frequency dependence of the spectral indices. A realistic Galactic field model would also lead to a spatially dependent suppression of the dust polarization fraction (Page et al. 2007; Miville-Deschenes et al. 2008).

The simulated maps are formed at each frequency ν using $\mathbf{d}_\nu = \mathbf{s}_\nu + \mathbf{n}_\nu$, where $\mathbf{n}_\nu$ is a realization of the *WMAP* noise. We consider both diagonal noise realizations, and full noise realizations including pixel-pixel and Q-U correlations, drawn from the *WMAP* $N_{\rm side}$=16 inverse noise matrices. These correspond to maps co-added by year and DA, as described in Jarosik et al. (2007); Hinshaw et al. (2008). The low resolution inverse noise matrices are not defined inside the processing mask, so we set the noise in these pixels to be large. Realizations are computed at each channel using SVD decompositions of the *WMAP* inverse noise matrices $\mathbf{N}_\nu^{-1}$, in antenna temperature. We then create $N_{\rm side}$=8 simulations, with 768 pixels, by degrading the $N_{\rm side}$=16 simulated maps and $\mathbf{N}^{-1}$ inverse noise matrices using inverse weighting.

We perform the Gibbs sampling using the four *WMAP* frequency bands K, Ka, Q, V (hereafter KKaQV). We do not include W band as standard, due to concerns about potential systematic effects (Hinshaw et al. 2008). For the diagonal noise case this requires of order 10,000 iterations for convergence. The chains are processed as described in §2.3 to obtain marginalized maps and errors for $\mathbf{A}_1$ (containing Q and U for CMB), $\mathbf{A}_2$ (synchrotron), $\mathbf{A}_3$ (thermal dust) and $\boldsymbol{\beta}$ (synchrotron spectral index).

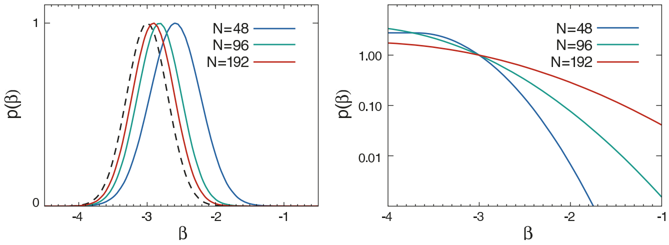

FIG. 1.— Left: For maps with $N_p = 768$ pixels and N_i (marked N in figure) synchrotron spectral indices with Gaussian priors of $\beta = -3.0 \pm 0.3$, the recovered index estimates are biased for simulations with no signal. The bias increases with the number of pixels sharing the same index (i.e., with decreasing N_i). Right: The phase-space prior that is added to produce unbiased estimates for the indices. In the rest of this analysis we use $N_i = 48$.

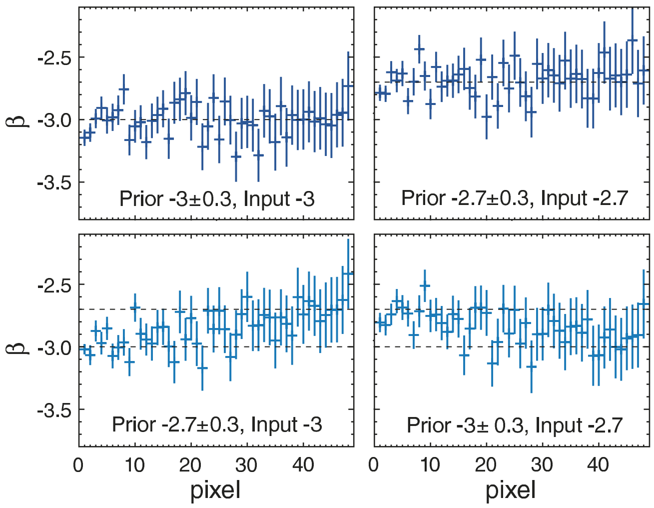

FIG. 2.— Marginalized mean and 1σ error bars for the synchrotron spectral index parameters for simulations with Gaussian priors of -3.0 ± 0.3 and -2.7 ± 0.3, and signal maps with synchrotron index -3.0 and -2.7. The pixels are ordered by increasing 1σ errors, with the highest signal-to-noise pixels on the left. When the prior matches the signal, shown in the top row, the estimated index values are unbiased. When the prior does not match the signal (bottom row), the input index value is recovered in the high signal-to-noise pixels, and the low signal-to-noise pixels tend to the prior.

3.1. *Phase-space prior*

To test for parameter bias, we sample the joint distribution for a noise-only simulation, drawn from the *WMAP* five-year noise maps, with the signal set to zero. The resulting marginalized distributions for the $N_i = 48$ spectral indices are close to Gaussian, but centered on $\beta = -2.6$. The Gaussian distribution best-fitting the samples is shown in the left panel of Figure 1. When the number of spectral index pixels is increased to 96, and 192, the recovered distribution is less biased, tending to the input value of $\beta = -3.0$. This effect can be explained as follows. Let us first take two pixels, each of which have an amplitude and a unique index parameter with a Gaussian prior centered on $\beta = -3$. If the volume of models with e.g., $\beta = -2$ is twice that of $\beta = -3$, this biases both index estimates a certain amount. If we now fit the two pixels with a common index parameter, there is four times the volume at $\beta = -2$ compared to -3, biasing the index estimate a larger amount. If there is a larger parameter space away from the prior central value, which is the case in our Galactic emission model,

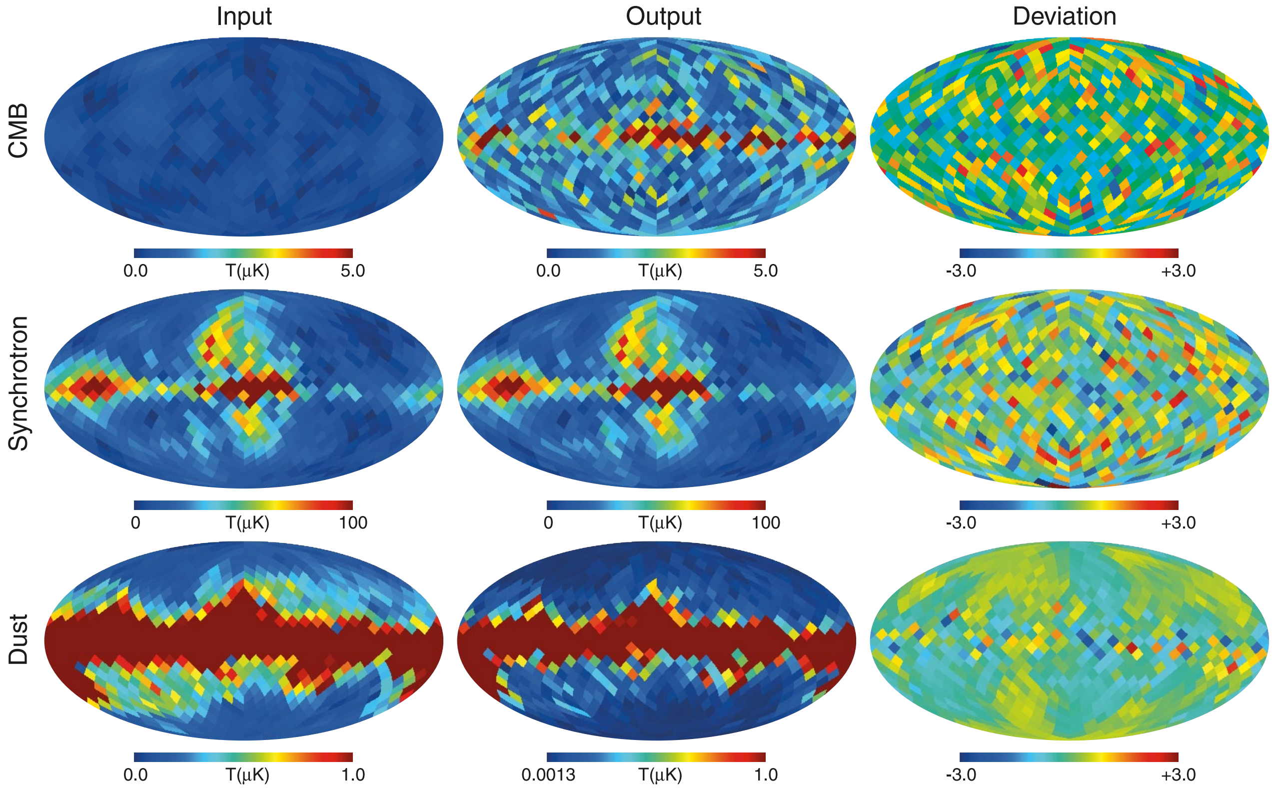

FIG. 3.— Comparison of input (left) and output (middle) component maps for a simulation with $N_{\rm side}$=8. The polarization amplitude $P = \sqrt{Q^2+U^2}$ is shown for the CMB (top), synchrotron at 23 GHz (middle), and dust at 94 GHz (bottom). The right panel shows the difference in standard deviations per pixel for the Q Stokes parameter. The dust component has a Gaussian prior on the dust Stokes parameters of $[Q,U](n) = 0 \pm 0.2 I_d(n)$, where $I_d(n)$ is the FDS dust intensity (see text), which reduces the deviation per pixel and leads to the structure in the difference map.

the bias will increase the fewer index parameters we use.

While there may be alternative parameterizations that avoid this problem, we choose to impose a parameter space prior that produces unbiased estimates. We can write the recovered distribution p' for each index parameter as the product of the input Gaussian prior and the effective phase-space volume v, with $p' = pv$. The additional phase-space prior we impose is then $1/v = p/p'$. These priors, modeled as Gaussian distributions, are shown in the right panel of Figure 1 for N_i=48, 92 and 192. These distributions are not exact, particularly at $\beta < -4$, but we check that the approximation is sufficient by resampling the noise-only distributions with the new prior, finding mean $\beta = -3.0$. We repeat the test for a Gaussian prior of -2.7 ± 0.3, and further test that this prior only weakly depends on the inclusion of W band.

We then test simulations with both signal and noise, for Gaussian priors of -3.0 ± 0.3 and -2.7 ± 0.3, and for two different signal maps with synchrotron index -3.0 and -2.7. The recovered mean and 1σ error bars are shown for the 48 index parameters in Figure 2. The pixels are ordered by increasing 1σ errors, such that the highest signal-to-noise pixels are shown on the left. As expected, when the prior matches the signal, shown in the top row, the estimated index values are unbiased. When the prior does not match the signal, the input index value is recovered in the high signal-to-noise pixels, and the low signal-to-noise pixels tend to the prior.

3.2. *Simulations with diagonal noise*

We now apply the method to simulations with signal and diagonal noise properties. Figure 3 shows the input and output polarization amplitude maps for the CMB, synchrotron, and dust components, derived from the Q and U maps, $P = \sqrt{Q^2+U^2}$, for the fiducial simulation with synchrotron index $\beta = -3.0$. The third column shows the difference in standard deviations per pixel for the Q Stokes parameter, $\delta = (Q_{\rm in} - Q_{\rm out})/\sigma_Q$. For the CMB maps the absolute difference between input and output maps is greatest in the Galactic plane where the foreground signal is high. However, since these effects are captured in the marginalized errors in the map, the deviation maps do not have a strong spatial dependence. The χ^2 for the map, $(\mathbf{A}_1^{\rm in} - \mathbf{A}_1^{\rm out})^T \mathbf{C}_1^{-1} (\mathbf{A}_1^{\rm in} - \mathbf{A}_1^{\rm out})$, is 1270 for 1536 pixels. This gives χ^2/pixel < 1, due to the prior on the dust amplitude. When the prior on the dust amplitude is removed, the goodness of fit of the recovered CMB maps is $\chi^2 = 1497$ (χ^2/pixel $= 0.98$), but the errors are significantly inflated. The synchrotron maps are recovered with χ^2/pixel $= 1.04$ for the Q and U maps. The dust maps are recovered with χ^2/pixel $= 0.24$, with structure apparent in the deviation map. This is due to the prior: far from the plane the signal-to-noise is low and the dust tends to the prior central value of zero. Removing the prior on the dust amplitude, the goodness of fit of the recovered dust maps is χ^2/pixel $= 0.97$, close to 1 as expected.

The optical depth computed from this simulation is $\tau = 0.091 \pm 0.019$ outside the P06 Galactic mask, with distribution shown in Figure 4. We test for bias by gen-

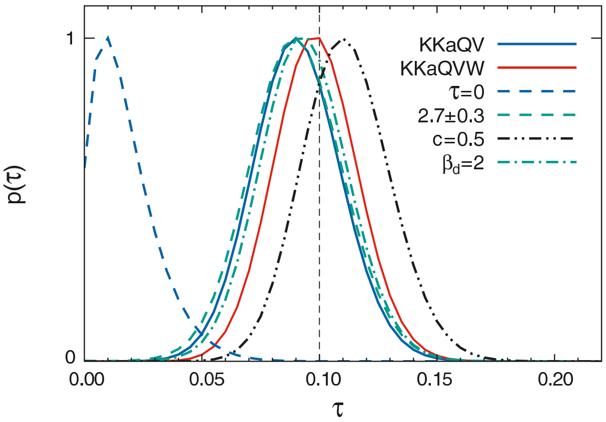

FIG. 4.— The distribution of the optical depth to reionization τ for simulations with five-year *WMAP* noise levels. The optical depth is recovered for an individual simulation with $\tau = 0.1$ for KKaQV and KKaQVW, and a $\tau = 0$ simulation is consistent with zero power. Changing the index priors to $\beta_d = 2$, or $\beta_s = -2.7 \pm 0.3$ have negligible effects on the recovered CMB power. Incorrectly modeling the synchrotron as a power-law for a simulation with an index that increases by $c = 0.5$ between 23 and 94 GHz increases τ by $\sim 1\sigma$.

erating 10 further diagonal noise and signal realizations of the model with $\tau = 0.1$, and find ensemble average of $\tau = 0.098$, consistent with the input but limited by small number statistics. We also test a simulation for KKaQV with no polarized CMB component. The recovered optical depth to be consistent with zero, shown in Figure 4. Adding W band (KKaQVW) we find $\tau = 0.098 \pm 0.017$.

In this ideal case the simulation matches the parameterized model, but in a realistic scenario the model will not perfectly describe the sky. For a Gaussian prior on the spectral index of $\beta_s - 2.7 \pm 0.3$, we find a negligible effect on τ, with $\tau = 0.094 \pm 0.020$. A larger increase of $\sim 1\sigma$ in τ, to 0.111 ± 0.019, is seen when the spectral index of the simulation shallows from -3.0 to -2.5 between K and W band, but is modeled by a pure power law. In this case the model does not remove enough synchrotron at high frequencies, leaving excess power in the CMB. For the thermal dust component we fix $\boldsymbol{\beta}_d = 1.7$ for all pixels in the fiducial case. Changing this to $\boldsymbol{\beta}_d = 2$ has a negligible effect on our results. Removing the dust prior altogether opens up long degeneracies between the dust and the CMB amplitudes, highlighting the importance of the dust intensity map to limit the polarized dust contribution. Modest changes of the dust polarization fraction prior to 15% or 25% have little effect on the estimated CMB signal.

3.3. *Simulation with full noise matrix*

When the full off-diagonal noise matrix is included we find of order 50,000 iterations are necessary for convergence. The χ^2 for the map computed using the full marginalized covariance matrix, $(\mathbf{A}_1^{\rm in} - \mathbf{A}_1^{\rm out})^T \mathbf{C}_1^{-1} (\mathbf{A}_1^{\rm in} - \mathbf{A}_1^{\rm out}) = 1220$ for 1536 pixels, consistent with the diagonal noise case ($\chi^2 = 1270$). The recovered spectral index distributions are consistent with the simulated values, and the estimated optical depth of a single simulation with input $\tau = 0.1$ is 0.110 ± 0.020. Testing a large set of simulations with full inverse noise matrices is beyond the scope of this analysis. To demonstrate the effect on the estimated CMB maps of marginalizing, Figure 5 shows two-dimensional marginalized distributions for a subset

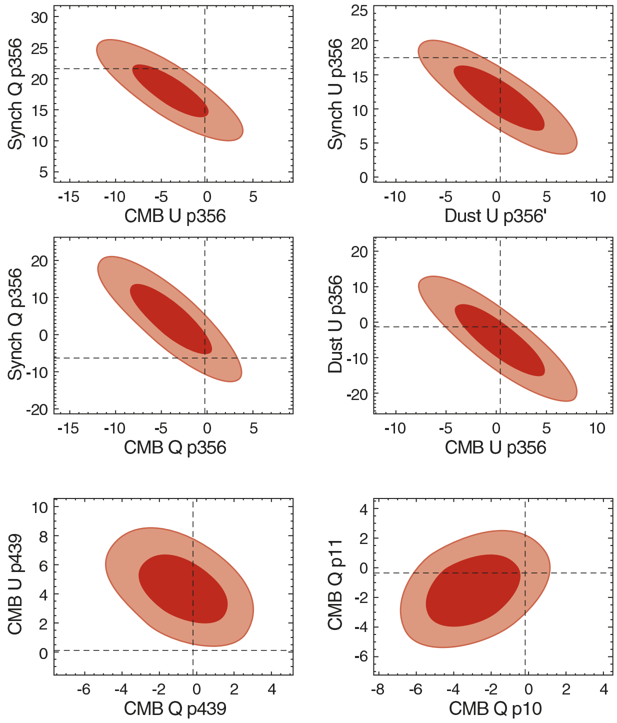

FIG. 5.— Marginalized 68% and 95% confidence levels for a subset of the A and β parameters. The top and middle panels show the correlation between the CMB, synchrotron and dust Q and U amplitudes (in μK) for an arbitrary single pixel (pixel 356 out of 768 using HEALPix nested ordering). The bottom panels show the correlation between Q and U for a single pixel (p439), and between two adjacent pixels (p10 and p11). By marginalizing, rather than finding the maximum likelihood, the error on the CMB amplitude is inflated to account for foreground uncertainty.

of parameters, for a single pixel and between pixels. The top and middle rows show the correlation between the CMB, synchrotron, and dust Q and U components within a single pixel. The one-dimensional marginalized error on the CMB Q and U amplitudes is larger than the error obtained if the foreground amplitudes are fixed at their maximum likelihood amplitudes. The bottom row shows correlations between Q and U components within a pixel, and between adjacent pixels. These inter-pixel correlations are small, but if ignored lead to recovered maps with incorrect noise properties.

4. RESULTS FROM *WMAP* DATA

We apply the sampling method to the five-year *WMAP* data, using low resolution coadded $N_{\rm side}$=16 maps and inverse noise matrices as the inputs, and then degrading to $N_{\rm side}$=8 as for the simulations. Figures 6 and 7 show maps of the mean values and 1σ errors for the marginalized CMB, synchrotron, and dust amplitudes.

4.1. *CMB polarization*

We first consider the CMB results. The noise patterns for both Q and U in Figure 7 are consistent with what we expect: in regions of low Galactic emission, the errors are dominated by instrumental noise. As the Galactic plane is approached, errors from foreground uncertainty begin to dominate, in particular where the dust contribution is most uncertain. This is a real advantage of the method: rather than imposing masks, the method inflates the errors where the foregrounds are brightest. As opposed to template cleaning, which produces CMB maps at each

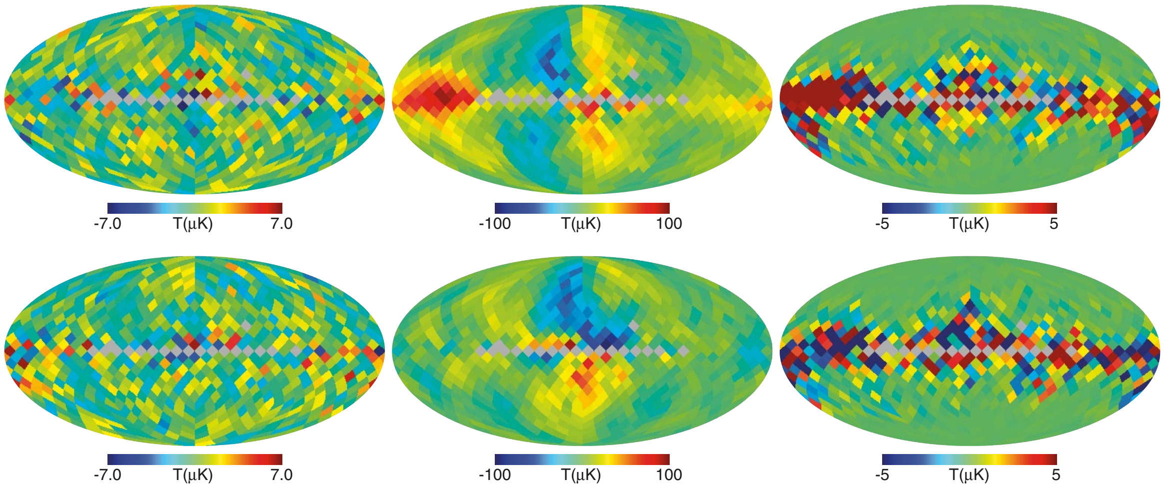

FIG. 6.— Low resolution polarized Q (top) and U (bottom) maps of the CMB, synchrotron, and dust emission, estimated from the five-year K, Ka, Q, and V band maps using Gibbs sampling. Pixels inside the processing mask are grey. The CMB maps (left panels, thermodynamic temperature) do not show significant Galactic contamination in the plane. The synchrotron amplitudes (center, antenna temperature), are defined at K-band (22.8 GHz), and are consistent with the total K-band maps, with high Q and U emission from the North Polar Spur, and high Q emission in the Galactic plane at longitude $110 \lesssim l \lesssim 170$. The dust amplitudes (right, antenna temperature) are defined at W-band (93.5 GHz), and have a Gaussian prior on Q and U of $0 \pm 0.2 I_d$ where I_d is the dust intensity.

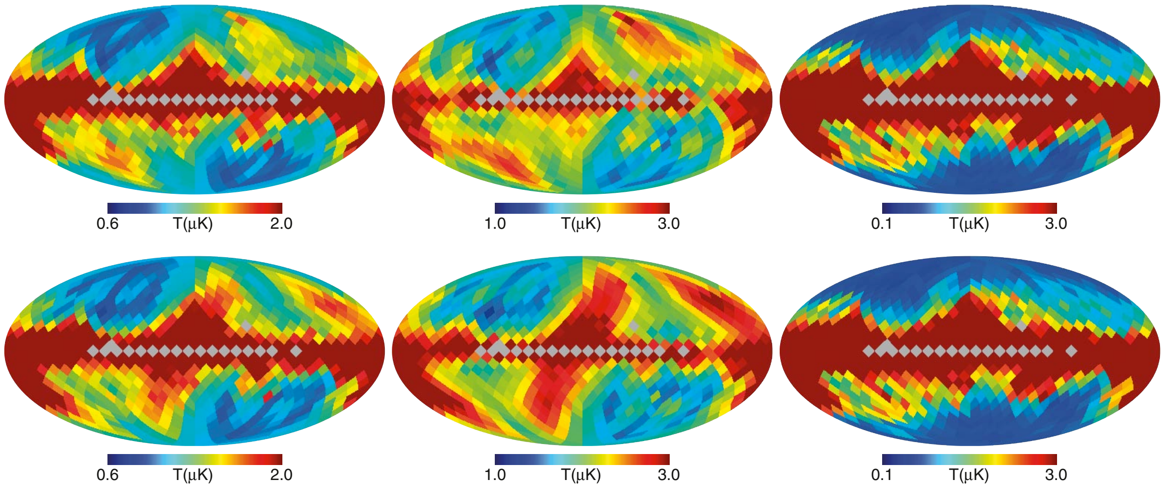

FIG. 7.— Estimated 1σ errors on the low resolution maps of the CMB (left), synchrotron (center), and dust (right) Q and U components, as shown in Figure 6. The CMB errors are more fully described by a covariance matrix, including pixel-pixel correlation and Q/U correlation, so the maps can be used for cosmological analysis. The errors on the dust maps (right) are dominated by the prior that limits the dust polarization fraction to 20%. The middle panels clearly show the two sources of uncertainty in our CMB polarization maps: detector noise in the ecliptic plane (which traces a sideways S in the map) and foreground removal uncertainties in the galactic plane.

frequency observed, this method recovers a single Q and U polarization map, and so has higher signal-to-noise than any of the individual template-cleaned maps. There is some indication of structure in the CMB signal, particularly in the Q Stokes map at the Galactic anti-center, and in the U map in the region of the North Polar Spur. This is consistent with noise. Outside the P06 mask the maps are morphologically similar to the template-cleaned CMB maps co-added over Ka, Q, and V bands.

We compare the power at each multipole, outside the P06 mask, to the template-cleaned case from the main analysis (Gold et al. 2008) in Figure 8. Using the method described in Nolta et al. (2008), at each multipole the conditional likelihoods is computed as a function of C_ℓ^{EE}, with all other multipoles held fixed, for $2 < \ell < 7$. The results are consistent, although this analysis finds more power at $\ell = 4$ and 5. Computing the likelihood as a function of τ we find $\tau = 0.090 \pm 0.019$ for the Gibbs-sampled maps outside the P06 mask, which is consistent with the results obtained through template cleaning, which give $\tau = 0.086 \pm 0.016$ for the KaQV data combination. Obtained using a different methodology and accounting for foreground marginalization, this adds confidence in the detection of the CMB E-mode polarization signal. The spatially varying synchrotron index appears not to cause a significant difference, as we obtain a similar mean when the synchrotron spectral coefficients are fixed at the best-fit values found in the template cleaning. We find similar limits on the optical depth when W band is included (KKaQVW), with $\tau = 0.085 \pm 0.017$. However, we choose not to use W band in the standard analysis, as discussed earlier. The Gaussian prior on the dust Q and U parameters does affect the CMB signal constraint: removing it significantly weakens the limit on the large-scale power, but changing it to e.g., 15% or 25% has little effect, consistent with tests on simulations.

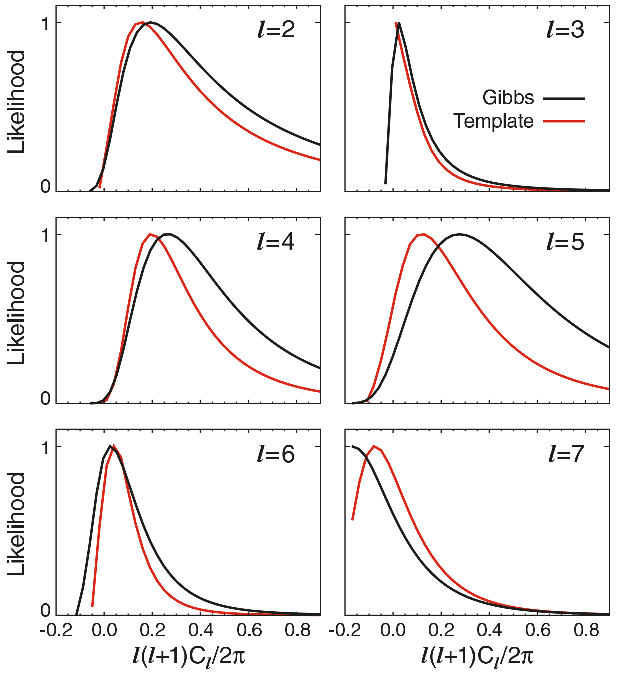

FIG. 8.— Conditional likelihoods for the CMB EE multipole moments estimated from the polarization maps described in this analysis (black), compared to the template cleaned maps described in Gold et al. (2008) (red). They are computed as in Nolta et al. (2008) by fixing all other C_ℓ values at the fiducial ΛCDM values. There is agreement between the two methods.

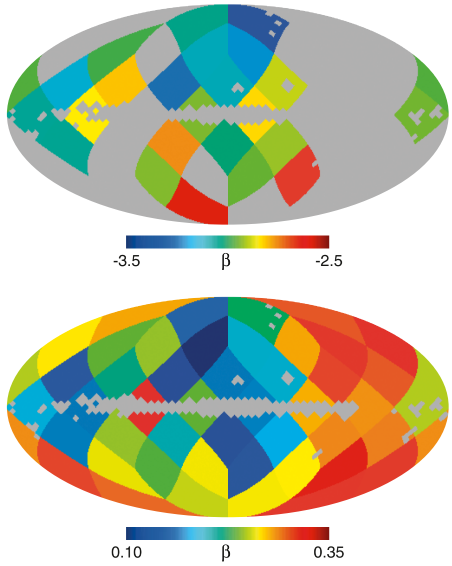

FIG. 9.— The estimated synchrotron spectral index (top), and 1σ errors (bottom), estimated in 48 HEALPix $N_{\rm side}$=2 pixels. A Gaussian prior of $\beta_s = -3.0 \pm 0.3$ is imposed in each pixel. In regions of low signal-to-noise (near the ecliptic poles), the prior drives the spectral index estimate, so we mask the index for pixels with $\sigma(\beta) > 0.25$. The mean index averaged over the unmasked pixels is -3.02 ± 0.04 for prior -3.0 ± 0.3.

A significantly tighter prior is not physically motivated, and could lead to bias in the recovered signal.

4.2. *Synchrotron polarization*

The synchrotron maps shown in Figure 6 are similar to the total K-band maps (Hinshaw et al. 2008). The difference between the estimated synchrotron amplitude, and the K-band amplitude, is $< 5\ \mu K$ outside the P06 mask, and $< 8\ \mu K$ in the Galactic plane. As observed in the three-year *WMAP* data (Page et al. 2007), the signal is dominated by emission from the North Polar Spur, marked on the microwave sky map in Hinshaw et al. (2007), as well as what is often known as the 'Fan region' (e.g., Wolleben et al. (2006)), centered on Galactic coordinates $l \sim 140$, $b \sim 5$. The synchrotron emission dominates the signal at low frequencies, and so the uncertainty in the synchrotron Q and U maps, shown in Figure 7, is dominated by instrument noise, with only a small contribution from marginalization in the Galactic plane. Figure 9 shows the mean synchrotron spectral index estimated in the 48 pixels, together with 1σ errors. In regions of low synchrotron signal-to-noise the index is driven by the prior, so we mask pixels with $\sigma(\beta) > 0.25$. There is a preference in the North Polar Spur and Fan region for an index of ~ -3: the index averaged over regions with $\sigma(\beta) < 0.25$ is -3.02 ± 0.04. The estimated indices of these pixels are also shown in Figure 10, sorted as in Figure 2 with increasing error to highlight the high signal-to-noise pixels on the left. Cutting the sky into high and low latitude at $b = 20$ degrees, the low latitude mean, -3.01 ± 0.04 is consistent with the high latitude -3.03 ± 0.06. This contrasts with the observed steepening of the index with latitude in Kogut et al. (2007) in the analysis of the three-year *WMAP* polarization data, although here we exclude part of the plane. This different result coming from an alternative analysis will be more easily addressed with higher signal-to-noise data.

An extrapolation of the Haslam 408 MHz synchrotron intensity maps to *WMAP* frequencies suggests that a shallower index is preferred in the plane, compared to the polarization, in the absence of anomalous dust. However, our estimated polarization index is consistent with the synchrotron intensity maps derived by the MEM method (Gold et al. 2008). Degrading the synchrotron component map in each band to $N_{\rm side}$=2, and fitting a power law to the data in K, Ka, Q, and V band for each pixel, the spectral index values are best-fit by a power-law with index $\beta = -3.1$ for the pixels at $b = 0$.

We check the estimate of the spectral indices by re-running the analysis with a synchrotron index prior of -2.7 ± 0.3. The estimated indices are compared pixel by pixel in Figure 10. The prior has only a small effect on the high signal-to-noise index estimates. The $\sigma(\beta) < 0.25$ pixel average in this case is -2.92 ± 0.04. The estimated CMB power is little affected by this change in prior, with $\tau = 0.092 \pm 0.019$.

4.3. *Dust polarization*

The dust polarization map has a low signal-to-noise ratio, particularly far from the plane, as we only fit data in the K-V bands. In these regions the prior dominates the estimate of the dust amplitude, making it hard to draw conclusions about the dust component. The error in Q and U is driven by the prior on the polarization amplitudes and so is morphologically identical to the FDS dust intensity map. This explains why the error far from the plane is low even though the dust is only poorly measured. The fractional polarization outside P06 is typically only 1-2%, where we use the degraded FDS dust map to trace intensity, and rises to ~10% in some regions of the plane. This is lower than the $\sim 4\%$ estimated in (Kogut et al. 2007; Gold et al. 2008). However, these

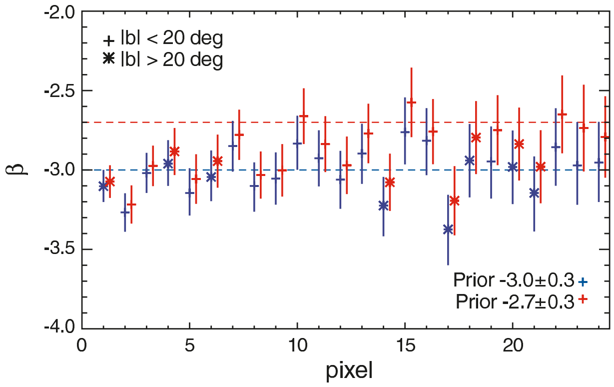

FIG. 10.— Marginalized mean and 1σ error bars for the synchrotron spectral index parameters with highest signal-to-noise for the five-year *WMAP* data, for Gaussian priors of -3.0 ± 0.3 and -2.7 ± 0.3. The pixels are ordered with increasing 1σ errors, with the highest signal-to-noise pixels on the left. The prior has only a small effect on the estimated indices.

maps are only estimated for $\nu \leq 61$ GHz, and in regions of low dust the prior prefers zero polarization. The fractional polarization estimate also assumes that the FDS map accurately traces the dust intensity in the *WMAP* frequency range. Inclusion of higher frequency data will allow us to learn more about the polarized dust.

5. CONCLUSION

We have used Bayesian parameter estimation to estimate low resolution polarized CMB maps, marginalized over foreground contamination. These may then be used as inputs for a likelihood analysis. The emission model is parameterized accounting for physical understanding of the Galactic emission. The method has been tested on simulated maps, and found to produce unbiased estimates for the signal power, quantified by the optical depth to reionization. With the five-year *WMAP* data we find a consistent result compared to template cleaning, with $\tau = 0.090 \pm 0.019$ from this method and 0.086 ± 0.016 from the standard template-cleaning method. This method captures the increase in errors where foreground uncertainty is larger, so depends less on a Galactic mask. Estimates of the polarized Galactic components indicate a synchrotron spectral index of order $\beta = -3.0$ in the Fan region in the Galactic anti-center, and the North Polar Spur area.

The *WMAP* mission is made possible by the support of the Science Mission Directorate Office at NASA Headquarters. This research was additionally supported by NASA grants NNG05GE76G, NNX07AL75G S01, LTSA03-000-0090, ATPNNG04GK55G, and ADP03-0000-092. EK acknowledges support from an Alfred P. Sloan Research Fellowship. This research has made use of NASA's Astrophysics Data System Bibliographic Services. We acknowledge use of the HEALPix, CAMB, and CMBFAST packages.

REFERENCES

Barnes, III, T. G., Jefferys, W. H., Berger, J. O., Mueller, P. J., Orr, K., & Rodriguez, R. 2003, ApJ, 592, 539
Beck, R. 2001, Space Science Reviews, 99, 243, kluwer Academic Publishers
Bennett, C. L., et al. 2003, ApJ, 583, 1
Berdyugin, A., Piirola, V., & Teerikorpi, P. 2004, A&A, 424, 873
Berdyugin, A., Teerikorpi, P., Haikala, L., Hanski, M., Knude, J., & Markkanen, T. 2001, A&A, 372, 276
Crutcher, R., Heiles, C., & Troland, T. 2003, in Lecture Notes in Physics, Berlin Springer Verlag, Vol. 614, Turbulence and Magnetic Fields in Astrophysics, ed. E. Falgarone & T. Passot, 155–181
Davis, L. J. & Greenstein, J. L. 1951, ApJ, 114, 206
Dobler, G. & Finkbeiner, D. P. 2007, ArXiv e-prints, 712
Draine, B. T. 2003, ARA&A, 41, 241
Draine, B. T. & Fraisse, A. A. 2008, ArXiv e-prints
Draine, B. T. & Lazarian, A. 1999, ApJ, 512, 740
Draine, B. T. & Li, A. 2007, ApJ, 657, 810
Duncan, A. R., Haynes, R. F., Jones, K. L., & Stewart, R. T. 1995, MNRAS, 277, 36
Dunkley, J., Bucher, M., Ferreira, P. G., Moodley, K., & Skordis, C. 2005, MNRAS, 356, 925
Dunkley, J. et al. 2008, ApJS
Eriksen, H. K., et al. 2006, ApJ, 641, 665
—. 2007, ApJ, 656, 641
Finkbeiner, D. P., Davis, M., & Schlegel, D. J. 1999, ApJ, 524, 867
Gelfand, A. E. & Smith, A. F. M. 1990, Jour. Amer. Statist. Assn, 85, 398
Geweke, J. & Tanizaki, H. 2001, Computational Statistics & Data Analysis, 37, 151
Gold, B. et al. 2008, ApJS
Gorski, K. M., Hivon, E., Banday, A. J., Wandelt, B. D., Hansen, F. K., Reinecke, M., & Bartlemann, M. 2005, ApJ, 622, 759
Han, J.-L. 2006, Chinese Journal of Astronony and Astrophysics, submitted (astro-ph/0603512)
Heiles, C. 2000, AJ, 119, 923
Hildebrand, R. H. & Dragovan, M. 1995, ApJ, 450, 663
Hill, R. et al. 2008, ApJS
Hinshaw, G., et al. 2007, ApJS, 170, 288
Hinshaw, G. et al. 2008, ApJS
Jarosik, N., et al. 2007, ApJS, 170, 263
Kamionkowski, M., Kosowsky, A., & Stebbins, A. 1997, Phys. Rev. D, 55, 7368
Knox, L., Christensen, N., & Skordis, C. 2001, ApJ, 563, L95
Kogut, A., et al. 2007, ApJ, 665, 355
Komatsu, E. et al. 2008, ApJS
Lawson, K. D., Mayer, C. J., Osborne, J. L., & Parkinson, M. L. 1987, MNRAS, 225, 307
Lewis, A. & Bridle, S. 2002, Phys. Rev. D, 66, 103511
Miville-Deschenes, M. ., Ysard, N., Lavabre, A., Ponthieu, N., Macias-Perez, J. F., Aumont, J., & Bernard, J. P. 2008, ArXiv e-prints, 802
Nolta, M. R. et al. 2008, ApJS
Page, L., et al. 2007, ApJS, 170, 335
Reich, P. & Reich, W. 1988, A&AS, 74, 7
Rybicki, G. B. & Lightman, A. 1979, Radiative Processes in Astrophysics (Wiley & Sons: New York)
Seljak, U. 1997, ApJ, 482, 6
Spergel, D. N., et al. 2007, ApJS, 170, 377
Spitzer, L. 1998, Physical Processes in the Interstellar Medium (Physical Processes in the Interstellar Medium, by Lyman Spitzer, pp. 335. ISBN 0-471-29335-0. Wiley-VCH , May 1998.)
Strong, A. W., Moskalenko, I. V., & Ptuskin, V. S. 2007, Annual Review of Nuclear and Particle Science, 57, 285
Strong, A. W., Moskalenko, I. V., & Reimer, O. 2000, ApJ, 537, 763
Uyaniker, B., Fürst, E., Reich, W., Reich, P., & Wielebinski, R. 1999, A&AS, 138, 31
Vallée, J. P. 2005, ApJ, 619, 297
Wandelt, B. D., Larson, D. L., & Lakshminarayanan, A. 2004, Phys. Rev. D, 70, 083511
Wolleben, M., Landecker, T. L., Reich, W., & Wielebinski, R. 2006, A&A, 448, 411
Wright, E. L. et al. 2008, ApJS
Zaldarriaga, M. & Seljak, U. 1997, Phys. Rev. D, 55, 1830